Title

Local Electric Field Effects on Water Dissociation in Bipolar Membranes Studied Using Core–Shell Catalysts

Journal

Chemistry of Materials, 36(24)

ISSN

0897-4756

Authors

Sarma, Prasad V
Kramar, Boris V
Chen, Lihaokun
et al.

Publication Date

2024-12-24

DOI

10.1021/acs.chemmater.4c02190

Local Electric-Field Effects on Water Dissociation in Bipolar Membranes Studied Using Core-Shell Catalysts

Prasad V Sarma[1], Boris V Kramar[2], Lihaokun Chen[1], Sayantan Sasmal[1], Nicholas P Weingartz[2], Jiawei Huang[1], James B Mitchell[1], Minkyoung Kwak[1], Lin X Chen[2], Shannon W Boettcher[1,3]*

[1]*Department of Chemistry and Biochemistry, University of Oregon, Eugene, Oregon, OR 97403, United States.*

[2]*Department of Chemistry, Northwestern University, Evanston, Illinois, IL 60208, United States.*

[3]*Department of Chemical & Biomolecular Engineering and Department of Chemistry, University of California, Berkeley, and Energy Storage and Distributed Resources Division, Lawrence Berkeley National Laboratory, Berkeley, CA 94720, United States.*

*Corresponding Author: boettcher@berkeley.edu

Abstract

The local electric field strength is thought to affect the rate of water dissociation (WD) in bipolar membranes (BPMs) at catalyst-nanoparticle surfaces. Here we study core-shell nanoparticles, where the core is either metallic, semiconducting, or insulating, to understand this effect. The nanoparticle cores were coated with a WD-catalyst layer (TiO_2 or HfO_2) via atomic layer deposition (ALD) and the morphology was imaged with transmission electron microscopy. Irrespective of the core material, these core-shell catalysts displayed comparable WD overpotentials, at optimal mass loading, despite the hypothesized differences in electric-field strength across the catalyst particle suggested by continuum electrostatic simulations. Substantial atomic interdiffusion between core and shell was ruled out by X-ray absorption spectroscopy, X-ray photoelectron spectroscopy, and diffuse-reflectance optical measurements. However, the optimal mass loading of catalyst was roughly one order of magnitude higher for the conductive and high-dielectric core materials than for the low-dielectric insulating cores. These findings are consistent with the hypothesis that electric-field screening within the core material focuses the electric field drop in-between particles such that larger film thicknesses can be tolerated. Collectively these data support the idea that it is the local electric field at the molecular level that controls proton-transfer rates and that the metal-core / dielectric-shell constructs introduced here modulate that field. Further materials and synthetic design may enable the optimization of the electric-field strength across the proton-transfer trajectory at the material surface.

Table of Contents Graphic

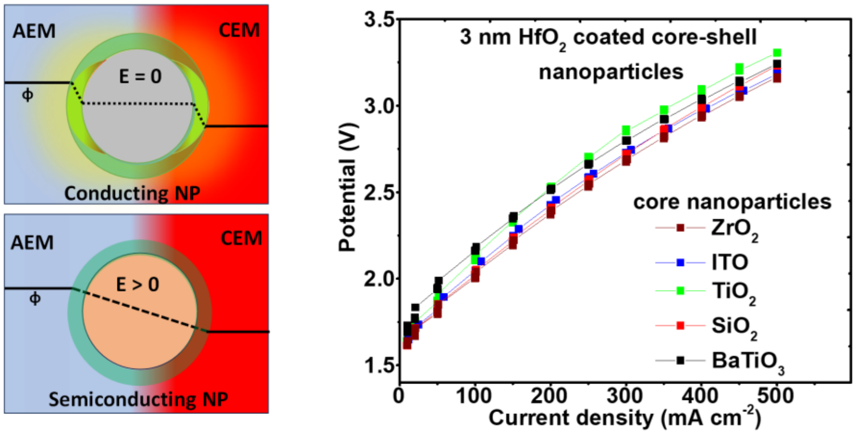

Introduction

A bipolar membrane (BPM) is comprised of two oppositely charged ionomer layers laminated together.[1] Typically, one is an anion-exchange layer (AEL; having positive fixed charge with mobile anions) and the other a cation-exchange layer (CEL; having negative fixed charges with mobile cations). BPMs uniquely enable electrochemical technologies to couple two different pH environments into a single device, for example, to enable optimized local pH of separated oxidation and reduction reactions. BPMs have been used in prototype fuel cells, flow batteries, photo-electrochemical cells, electrolyzers and for resource recovery.[2–5] BPMs can also be used to generate acid and base from salt at high efficiency using electrodialysis,[6] as well as enabling control of ion transference to block unwanted ion crossover in CO_2 or impure-water electrolyzers.[2,7] In water electrolysis, they offer possibly useful alternatives to monopolar hydroxide or proton membranes by providing an acidic environment at the cathode for fast hydrogen-evolution kinetics and a basic environment at the anode for oxygen evolution on non-precious metal oxides.[8]

Under applied reverse bias, the bipolar CEL|AEL interface is depleted of ions and the space charge around the interface increases in width. For a bipolar membrane at equilibrium, the electrochemical potential of any species *j*, $\underline{\mu}_j$, is constant as a function of position. In analogy to a semiconductor *pn* junction, this equilibrium results in opposed gradients in the chemical potential of protons and of electric potential acting on the protons.

The change in the electrochemical potential of protons and hydroxide across the interface ($\Delta\underline{\mu} = F \times$ applied overvoltage, where F is Faraday's constant) drives ionic current and depletes the junction region of these ionic carriers. Thus, the water dissociation (WD) reaction proceeds at the BPM interface in the forward direction to generate ionic carriers at a steady state, and the local concentrations and kinetics determine the reaction rate.

$$2H_2O \underset{k_1 \rightarrow}{\overset{k_{-1} \leftarrow}{}} H_3O^+ + OH^- \tag{1}$$

The rate constant k_{-1} and k_1 describes the rate of recombination and dissociation respectively. We thus define the WD overpotential as a function of current *i* as:

$$\eta_{wd} = \frac{\Delta\underline{\mu}_{H^+}}{F} = \frac{\Delta\underline{\mu}_{OH^-}}{F} = F\left(\Delta\phi_{BPM}(i) - \Delta\phi_{BPM,eq}\right) \tag{2}$$

The term j represents the type of charge species, $\Delta\phi_{BPM}(i)$ is the electrostatic potential across the BPM at a current i, and $\Delta\phi_{BPM,eq}$ is the equilibrium electrostatic potential ($i = 0$). The WD reaction is followed by the transport of dissociated products (H^+ and OH^-) away from the BPM junction to respective electrodes along the direction of the electric field, given by (in the dilute-limit approximation where species are not interacting)[9]:

$$J_j(x) = -\frac{C_j D_j}{RT}\frac{d\underline{\mu}_j}{dx} \tag{3}$$

The variables $\underline{\mu}_j$, C_j, D_j, and J_j are electrochemical potential, concentration, diffusion coefficient, and flux of species j. We note that to accurately model species transport in BPMs, concentrated electrolyte theory is probably needed.[10]

At the BPM junction where the AEL and CEL meet, a strong electric field develops, generated by oppositely charged uncompensated fixed charges on the ionomer in the individual membranes. This electric field will interact with dipolar species like water molecules. The electric field may accelerate WD kinetics that proceed via protonation/deprotonation reactions with weak acidic or basic groups on the membrane or with intentionally added catalysts.[11] The magnitude of this hypothesized effect has been estimated using Onsager's theory of the second Wien effect where the electric field shifts the equilibrium towards dissociation and increases the forward WD rate constant k_1 in Eq. (1) above.[12] The recombination rate constant (k_{-1}) is assumed to be constant and limited by diffusion, although there is no direct experimental evidence for this.[11,12] A *pn* junction analogy with an abrupt junction model, where the electric-field-enhancement effect (EFE) is attributed to the higher WD kinetics, has been used to analyze the performances of BPMs, although again without experimental support.[13–15]

The addition of an interfacial WD catalyst is practically essential to achieve high current densities (e.g. 0.1 to 1 A cm^{-2}) with low η_{wd} less than a few tenths of a volt. Certain metal oxides efficiently catalyze WD, and these catalyst layers also modify the structure of the BPM interface.[8,16] The catalyst-membrane interface properties (thickness, catalyst dispersion) and composition, etc., influence the resistance and overall performance of BPM electrolyzers.[9] Simply, catalyzed BPM dramatically increases WD kinetics, but the addition of a WD catalyst increases the junction thickness which modifies the junction electric field (**Figure 1**).

We hypothesize that the electric-field distribution across the catalyst-coated interface depends on the nature of the catalyst, where metallic catalyst screens and focus the electric field (causing a large local electric-potential gradient) while semiconductors, and insulators, cause a more-gradual drop in electric potential. The relative contributions from EFE and catalytic pathways, and how they interact to determine the reaction kinetics, remains unclear. Comparing the WD kinetics of a pristine (smallest junction width and thus highest electric field) and catalyzed BPM (with electric field spread over the width of the catalyst layer), illustrates that surface catalytic pathways are essential for high performance, although these pathways are almost certainly accelerated by the local electric field.[17] To analyze this hypothesis, one could systematically modify the overall electric field across the WD catalyst by controlling the concentration of uncompensated fixed charges in the membranes, while maintaining an identical WD catalyst. However, such modifications alter the chemistry of the BPM interface and transport properties of the ionomers, convoluting analysis.[18]

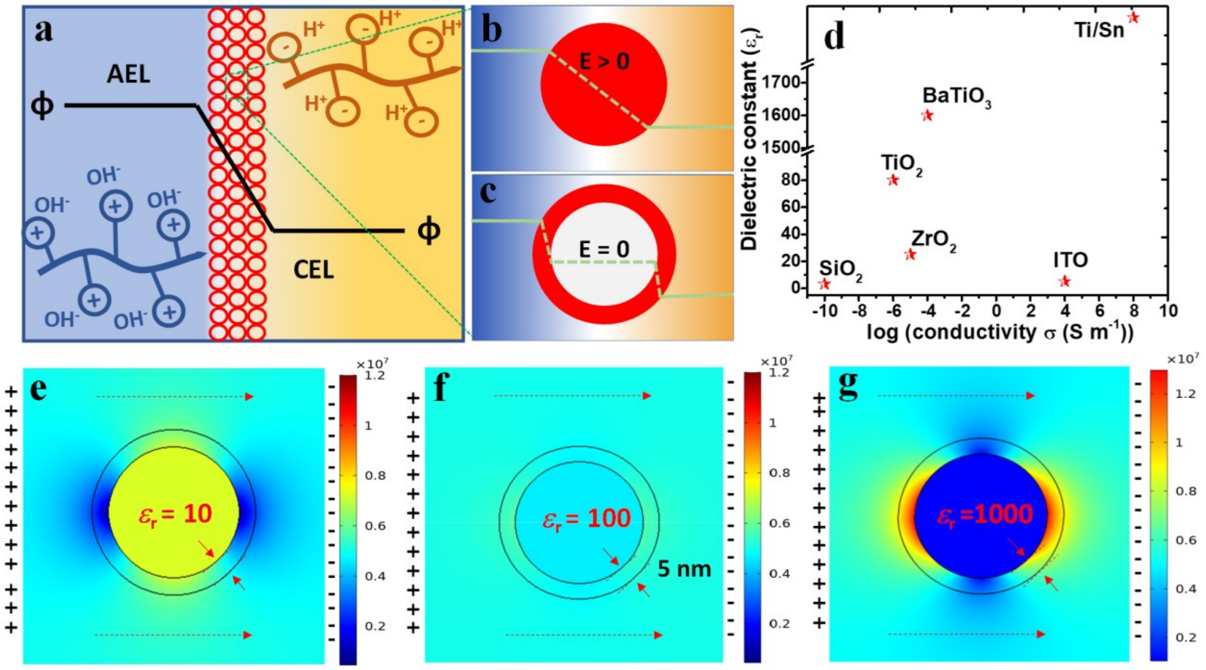

Figure 1: **Schematic of electric potential gradient in BPM interface** (a) Catalyzed bipolar membrane, (b) hypothesized electric potential across a (b) solid nanoparticle and (c) core-shell nanoparticle. The potential gradient is steeper if the core material is electronically conducting so that the electric field inside will be shielded by mobile charge carriers. (d) Dielectric constant vs. electronic conductivity of various core nanoparticles. Simulation models (COMSOL) for core-shell nanoparticles having relative dielectric constants of (e) 10, (f) 100, and (g)1000, under an applied electric field in units of V/m.

Here, we introduce core-shell nanoparticles as WD catalysts as a strategy to alter, and study the effect of, the electric field profiles across the bipolar junction (Figure 1). We investigate how core electric conductivity and dielectric constant of the catalyst nanoparticles effects WD kinetics. We hypothesized that the conductive or high-dielectric core material could concentrate the electric field to the WD catalyst surface via screening of the field within the core. Nanoparticles with varying dielectric properties, including metals, insulators, and semiconductors, were coated with a WD-catalyst layer (TiO_2 or HfO_2) via atomic layer deposition (ALD). The thickness of the WD catalyst shell was chosen and maintained uniformly across all core materials under study in such a way that there are negligible chemical interactions (such as interdiffusion/doping) between the core material and the outermost layer of the WD catalyst, which might modify the chemistry of the catalytic system. Such possible surface-chemical modifications to the outermost WD catalyst layer were ruled out by analyzing the coordination environment of the catalyst shell across different core materials using X-ray absorption spectroscopy (XAS). We also note that the electric field and catalytic effects on the WD rate are entwined at the microscopic level. For example, for a sufficiently fast WD catalyst, the local electric field will be maintained at its equilibrium value. In this study, we worked to keep the catalytic sites (hypothesized to be proton donor and acceptor sites on the metal-oxide surface) constant while varying the local electric field strength both at equilibrium and under an applied overpotential. We then modified how the electric field is distributed within the porous nanoparticle WD catalyst layer where conductive cores result in more of the electric field residing in the water, and insulating cores resulting in more of the electric field residing in the solid inorganic core.

The article is arranged as follows; we first developed a simple electrostatic model that informs the EFE, followed by material synthesis and characterization. Then, the catalytic WD performance of the core-shell catalyst systems in BPM water electrolyzers (BPMWEs) is reported. Finally, we discuss the shortcomings of the chosen model systems followed by the directions for future studies.

Experimental Section

Material Synthesis and Characterization: Nanoparticles including SiO_2 (20-30 nm), ZrO_2 (20-30 nm), indium tin oxide 90:10 (20-70 nm), $BaTiO_3$ (50 nm), tin (50 nm), titanium (30-50 nm) and silicon (30-50 nm) nanoparticles were purchased from US Research Nanomaterials. The shell coating of TiO_2 or HfO_2 was performed using a Savannah 300 atomic layer deposition (ALD) system. Tetrakis(dimethylamido) titanium (TDMAT) and ultra-pure water were used as precursors for TiO_2 deposition. Similarly, tetrakis(dimethylamido) hafnium and ultra-pure water were used for HfO_2 deposition. The ALD was performed at a temperature of 250 ºC for both TiO_2 and HfO_2 deposition. The thickness of the deposited layers was controlled by controlling the number of ALD cycles. After coating, the materials were annealed under air to form crystalline oxide phases (450 ºC for TiO_2 and 600 ºC for HfO_2).

Gas diffusion layers (GDLs) coated with anode catalyst were prepared with Co_3O_4 (30-50 nm) nanoparticles (US Research Nanomaterials) sprayed on stainless steel 25AL3 (Bekaert Bekipor®) from ionomer ink. The cathode is similarly prepared from platinum back (high surface area, Fuel cell store) onto Toray carbon paper 090 (wet-proofed value pack, Fuel cell store). Procedures are provided in the supporting information section 1: Methods.

A Bruker D2 Phaser benchtop diffractometer was used to collect XRD patterns for the nanoparticles. Transmission electron microscopy images were collected using an FEI Titan 80-300. X-ray photoelectron spectroscopy (XPS) characterization was with an ESCALAB 250 (Thermo Scientific). Diffuse Reflectance UV-Vis data were collected on a Shimadzu 2600 spectrophotometer with integrating sphere attachment (Shimadzu ISR-3100). Scanning electron microscopy (SEM) imaging was carried out using a ZEISS Ultra tool. Surface-area measurements were performed at 77 K by N_2 adsorption-desorption analysis using Micrometrics ASAP 2020 analyzer.

The apparent electronic conductivities of nanoparticles were measured using a two-electrode setup. A pellet was made with nanoparticles using a die and press (Quick Press Sigma-Aldrich®) and a homemade polyether-ether-ketone (PEEK) collar. The thickness of the pellet is measured using a digital vernier caliper. The metal sheets on the press are used as the two electrical leads to measure the current-voltage response collected between ±0.1 V at 5 mV s^{-1}, while the nanoparticle powder is kept under a static pressure of ~ 5,000 psi. The curve is fitted to a line to extract the electronic resistance.

Water dissociation catalyst coating: The WD catalysts (core-shell nanoparticles) were dispersed in isopropyl alcohol: de-ionized water (1:1 by weight) under sonication. The WD catalyst ink was spin coated onto Nafion 212 membrane at 3000 rpm for 30 s. Afterwards, the WD-catalyst-coated CEL is covered with Versogen AEL (PiperION-A40-HCO3; TP-85, 40 μm) during BPM assembly. Different concentrations of catalyst inks were used for spin coating to vary the WD catalyst loading in the membrane. Some dispersions (for ex. $BaTiO_3$) were spray coated onto the membrane, due to the low dispersibility of the solute (see Supporting Information Section 1: Methods).

BPM Electrolyzer assembly and electrochemical measurements: A modified Single Cell Fuel Cell Hardware Assembly, Fuel Cell Technologies was used for electrolyzer testing. Stainless steel and graphite flow fields were used for water delivery to the anode and cathode, respectively. The active area is kept as 1 cm^2 by using several gaskets of varying thickness (PET, McMaster Carr; with total thickness of 0.032" on the cathode side, and 0.040" thickness on anode side). Sintered titanium frits electroplated with 1 µm Pt, (1 cm × 1 cm, Baoji Yinggao Metal Materials Co., Ltd.) were used as spacer layers. Pt-black-coated carbon Toray paper is placed on top of titanium spacer, catalyst facing up. Later, the catalyst coated BPM is placed on top of the cathode catalyst layer, with the Nafion 212 CEL facing the cathode. After placing several gaskets of thickness 0.040", a Co_3O_4 anode GDL was placed on the membrane, where the Co_3O_4 catalyst facing the Versogen AEL. The titanium spacer was added on top of the anode GDL and finally, the anode flow field and current collectors were placed on top to complete the stack. The stack was then bolted together and tightened by using torque wrench (50 inch-pounds). De-ionized water heated to 60 ºC was fed into both anode and cathode from a temperature-controlled reservoir of water (~15 L).

The electrochemical measurements were performed using a Biologic VSP-300 potentiostat. The cell current-voltage measurements were started after the cell reached 55 ºC. Impedance spectroscopy (EIS) was performed at frequencies between 0.1 Hz and 1 MHz with an amplitude of 5 mV.

X-ray absorption spectroscopy measurements*:* XAS data was collected at the Ti K-edge (4.966 keV) at Beamlines 12-BM (all TiO_2 @ SiO_2 data) and 5-BM (all TiO_2 @ ZrO_2 data) at the Advanced Photon Source at Argonne National Laboratory. All measurements were conducted in fluorescence mode.

Results and Discussion

Electrostatic Model. We used simulations (in COMSOL) to model the electric-field distribution near the boundaries of the core-shell nanoparticles in the direction of the field (Figure

1e-g), assuming the applied potential is completely utilized for generating an electric field across the BPM interface. In this calculation, no co-ions or dissociated products are included, and the continuity equations together with Poisson's equations were solved under the prescribed boundary conditions. The core dielectric constants were varied and the shell dielectric constant was held at 80 (as that of rutile TiO_2) and the thickness as 5 nm. The electric field enhancement is larger (~3 times from the background values) for a high dielectric core system compared to the low dielectric core while maintaining the identical shell material. Such field enhancement is thought to polarize the water dipole and order the water molecule on the catalyst surface in ways that may promote proton transfer to/from the surface.[11,12,17]

Catalyst imaging and spectroscopy characterization. We chose different nanoparticles (SiO_2, ZrO_2, ITO, $BaTiO_3$, Sn, Si, and Ti) having a range of electronic conductivity and dielectric properties as the core. The various properties of nanoparticles under study are listed in Table S1 (*supporting information*) and the log (electronic conductivity) *vs.* dielectric constant of these nanoparticles is shown in Figure 1g. Different thicknesses (1 nm – 5 nm) of TiO_2 was coated onto core nanoparticles using ALD. The transmission electron microscopy (TEM) images (**Figure 2** and supporting information Figure S2-S6) show a conformal coating of 4-5 nm TiO_2 shell over the nanoparticle cores. The oxidation state of Ti in these core-shell systems was analyzed via X-ray photoelectron spectroscopy (XPS) given in supporting information Figure S7. The oxidation state of Ti remains identical in all the samples with a slight variation in peak width, perhaps indicating a larger degree of site heterogeneity. The optical absorbance measured by diffuse reflectance UV-Vis spectroscopy was performed on the core-shell nanoparticles to derive the optical band-gap of the WD catalyst shell, 4 nm TiO_2 (refer Figure S8). The measured optical band gap of a 4 nm thick TiO_2 shell was similar across different core-shell systems. Thinner layers displayed larger bandgaps, likely due to confinement effects (Figure S8-S9: Diffuse reflectance analysis).[19]

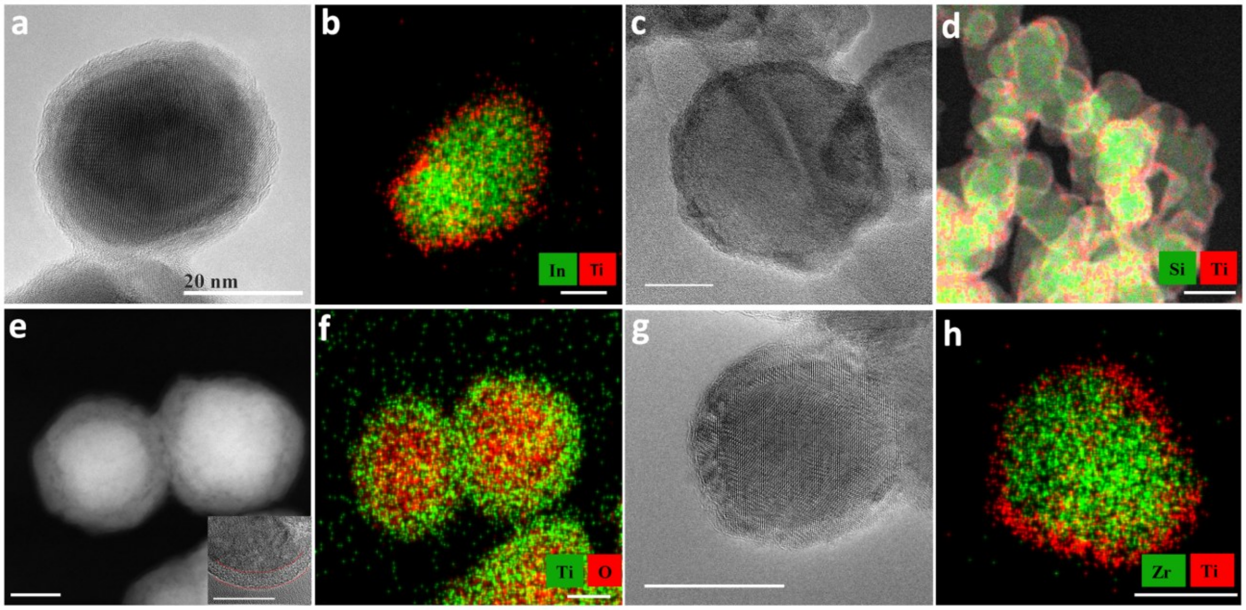

Figure 2: TEM and EDX mapping images of TiO_2-coated core-shell particles. (a-b) TiO_2-coated ITO (c-d) TiO_2 -coated silicon nanoparticles. (e-f) TiO_2-coated titanium (g-h) TiO_2-coated ZrO_2 nanoparticles. The colors red and green in the mapping image represent shell and core materials, respectively. All the scale bars in the figures are 20 nm.

The structure and Ti coordination environment in selected core-shell composites were investigated with XAS.[20] As it is likely that the 1 nm (and even 4 nm) thick shell does not match the bulk TiO_2 crystal XAS, comparisons were made to nanoscale ~30 nm in diameter anatase and rutile samples (**Figure 3**). Due to limitations in beam time, we focused the XAS analysis on the TiO_2-coated SiO_2 and TiO_2-coated ZrO_2. The SiO_2 is amorphous with a very large surface area (~185 m^2 g^{-1}) while the ZrO_2 is crystalline with a smaller surface area similar to the other core materials reported here (~30-60 m^2 g^{-1}). It is interesting to observe that WD performance in the BPM were similar for the 1-nm and 4-nm TiO_2 coating on the ZrO_2, and the 4-nm coating of TiO_2 on SiO_2, but that the 1-nm TiO_2 coating on the SiO_2 was a dramatically worse WD catalyst, as discussed below.

The Ti-K edge features of the 4-nm TiO_2 shell coated on both SiO_2 and ZrO_2 core (Figure 3a) were analyzed; the pre-edge (Figure 3c) and post-white line (Figure 3b) features of both catalysts appear to be match with nanoparticle rutile phase reference sample (data processing and fitting are in Section S3). The XAS of TiO_2 (4-nm thick) over both SiO_2 and ZrO_2 display a similar coordination environment suggesting little intermixing between core and shell. Extended X-ray absorption fine structure (EXAFS) spectra (Figures 3d, 3h), obtained by performing the Fourier transform onto the post-edge region of the X-ray absorption spectra, also indicate a similar coordination environment for 4-nm TiO_2-coated shells. EXAFS fitting was carried out on these samples to estimate the nearest-neighbor coordination numbers for the Ti – O and Ti – Ti scattering paths. Details on the fitting routine and representative figures can be found in the SI (Section S3, Figure S10 – S14: EXAFS fitting). The results are in Table 1 and are compared to reference structures for anatase and rutile.[21]

In a 1-nm TiO_2-coated SiO_2 core-shell system (TiO_2@SiO_2), the white line features for the 1-nm-thick shell were not well fit with any ordered TiO_2 crystalline phase. The pre-edge features are distorted, which indicates a low degree of crystalline order around the Ti centers. Similar sharpened pre-edge features have been observed previously for a range of TiO_2/SiO_2 glasses and gels, which may indicate that in the 1-nm TiO_2 @ SiO_2 sample a significant fraction of the Ti centers are intermixed with the SiO_2.[22–25]

In contrast, the 1-nm TiO_2 @ ZrO_2 sample does maintain a rutile-like structure of the TiO_2 shell. We conclude that the effect imposed by the core onto the structure of the TiO_2 layer is different between the two supports, likely owing to the degree to which the TiO_2 unit cell matches the respective unit cells of SiO_2 or ZrO_2. However, from XANES, EXAFS, diffuse reflectance, and XPS analysis on a 4-nm-thick TiO_2 shell on different cores, we conclude that the catalyst bonding and electronic structure is similar regardless of the core.

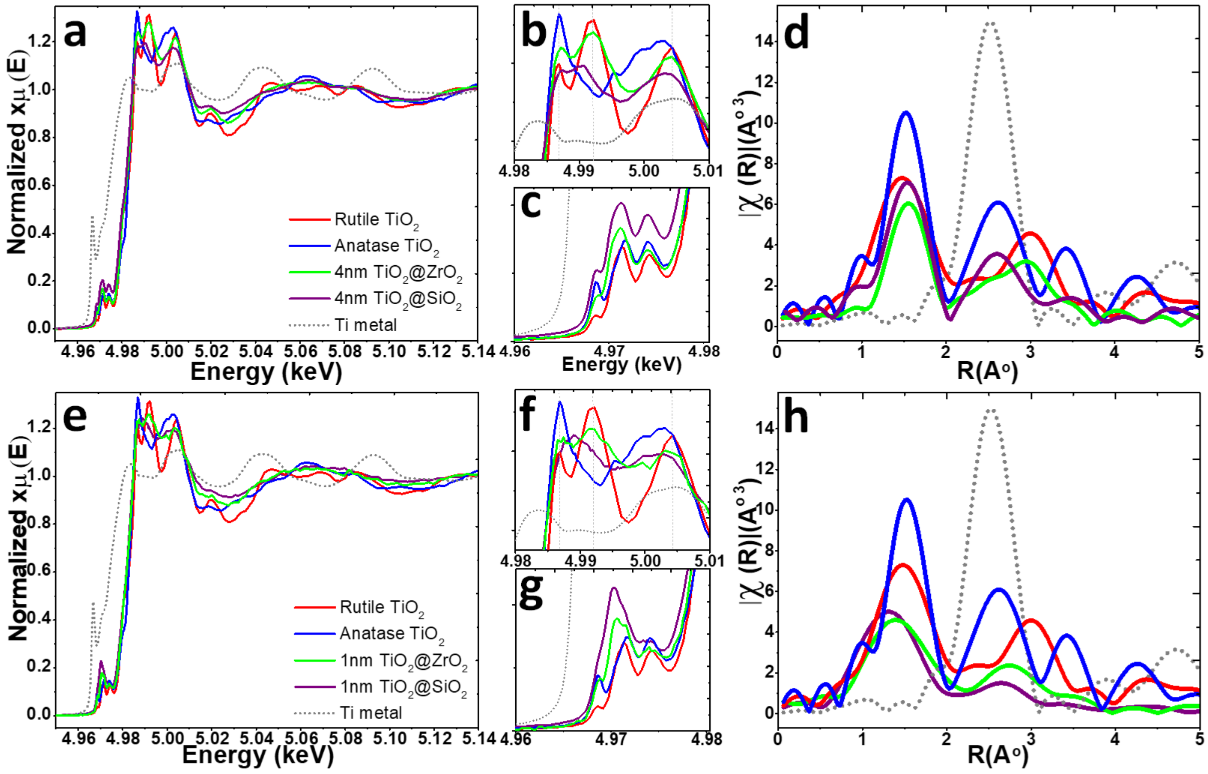

	Expected: anatase	Expected: rutile	4 nm TiO_2 @ ZrO_2	1 nm TiO_2 @ ZrO_2	4 nm TiO_2 @ SiO_2	1 nm TiO_2 @ SiO_2
Ti – O, [1]	6.0	6.0	~6	5.9	~6	5.3
Ti – Ti, [2]	4.0	2.0	2.0	2.0	3.4	1.5
Ti – Ti, [3]	4.0	8.0	1.3	1.2	2.5	N/A[a]

[a] Parameter space is not large enough to include this path in fitting.

Figure 3. X-ray absorption spectra collected from selected samples, plotted with relevant references. (a) XANES region, (b) white-line close-up, (c) pre-edge close-up, and (d) the k^3 weighted Fourier transform magnitude of the EXAFS region for 4-nm TiO_2 coated SiO_2 and ZrO_2 systems. (e-h) XAS from 1-nm TiO_2 coated core-shell nanoparticles. (e) XANES region, (f) white-line close-up, (g) pre-edge close-up, and (h) the k^3 weighted Fourier transform magnitude of the EXAFS region for 4-nm TiO_2 coated SiO_2 and ZrO_2 systems. The table at the bottom gives the fit single-scattering path coordination numbers for the nanoscale anatase, 4-nm, and 1-nm TiO_2-coated nanoparticles.

Water dissociation kinetics of core-shell catalysts. The BPM electrolyzer performance was analyzed using these core-shell nanoparticles as WD catalysts. BPM electrolyzers were operated at 500 mA cm^{-2} and the total cell voltage was monitored, as shown in Figure 4a, for the range of core catalyst materials all coated by 4-nm of TiO_2. The galvanostatic EIS data and associated fits for the same core-shell catalyst BPM electrolyzers given in Figure 4b. Both data sets illustrate the similar charge-transfer resistance across various core-shell systems, as discussed further below. We chose to compare η_{wd} at 500 mA cm^{-2} where for all the catalysts the change in electric potential across the AEL/CEL junction is large and significant effects due to how the catalyst modulates the local electric fields were hypothesized to be evident.

The electrolyzer voltage was similar for all the various core-shell systems with a 4-5 nm TiO_2 catalyst shell coating, except SiO_2/silicon core with 200-300 mV higher cell voltages. SiO_2 had a surface area (185 m^2/g) five times higher than the other cores studied, which may be connected to the high voltage, perhaps due to inability to of the ALD reaction to fully coat small internal porosity.

We also studied hafnium oxide (HfO_2) as an alternative to TiO_2 WD catalyst shell. HfO_2 has a lower electronic conductivity (and is thus used as a gate dielectric) and has a smaller dielectric constant. We hypothesized HfO_2 might have lower WD activity but be more sensitive to the electronic properties of the core. The characterization details (Figures S15-S19: TEM analysis, Figure S20: diffuse reflectance, and Figure S21: XPS) are shown in supporting information section 4. The BPM electrolyzer performance of all these catalysts, at optimal mass loading, were found to be similar (even with a thin HfO_2 coating of ~ 3 nm) irrespective of the core material (Figures 4c and d). However, there were significant differences in the optimal mass loading across the series (discussed in more detail below). For reference, the BPM electrolyzer performance of pristine nanoparticles, reference catalysts (TiO_2@TiO_2, TiO_2@Ti, HfO_2@HfO_2), various core-shell catalysts, and uncatalyzed BPM were given in Figure S22-S31.

We also analyzed the possibility of surface reconstruction of the WD catalyst during operation, which could complicate the data interpretation. We performed *operando* XANES analysis of the WD catalyst using a custom electrolyzer assembly (the schematic and the photographs of the electrolyzer are given in supporting information Figure S32). *Operando* X-ray absorption spectra from the WD catalyst (4-nm TiO_2 coated SiO_2) are collected at different current densities, and open circuit conditions, shown in Figure S32d. The Ti K pre-edge as well as the post-edge features were analyzed in the XANE spectra (Figure S32d). The spectral features confirm that the coordination environment Ti remains unchanged before, during, and after the electrolyzer run, which rules out large changes to the WD catalyst.

For the 3-nm HfO_2-coated nanoparticles, we used impedance analysis to decouple the η_{wd} from the total cell voltage (Figure S33) and assess how the core electronic properties might influence WD on the surface. The impedance spectra at different current densities were collected, and the high-frequency semicircle is taken to include $R_s + R_{wd}$, where R_s is the series resistance and R_{wd} is the water dissociation resistance.[17] The η_{wd} values are then calculated from:

$$\eta_{wd} = \int_0^j R_{wd}(j)dj \tag{4}$$

We found that the R_{wd} is a function of the applied current density (j), i.e., the resistance lowered with driving force, deviating from the ideal Ohm's law.

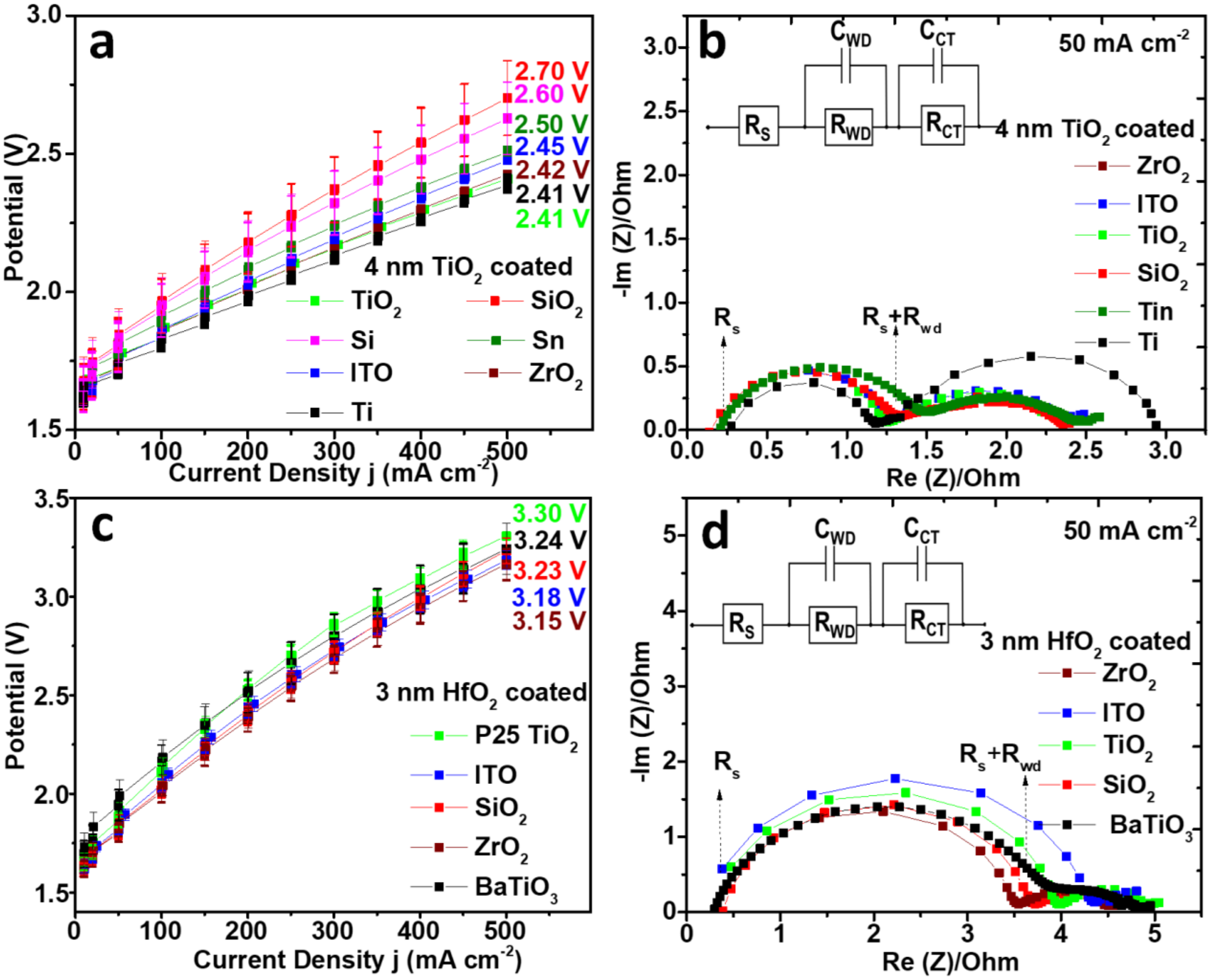

Figure 4: Polarization curves and impedance analysis. The WD catalysts were spin-coated onto the Nafion 212 membrane, and the data for optimal loading conditions is shown for all the catalysts under study. (a) BPM electrolyzer polarization curve with different core-shell nanoparticles as WD catalysts. (b) Galvanostatic EIS data (at 50 mA cm^{-2}) was obtained using 4 nm-thick TiO_2-coated core-shell nanoparticles. (c) Polarization curve and (d) galvanostatic EIS data collected at 50 mA cm^{-2} for HfO_2-coated core-shell nanoparticles.

The overpotential measured from EIS is shown in supporting information Figure S33f for HfO_2-coated core-shell nanoparticles. The measured η_{wd} for all the HfO_2-coated core-shell nanoparticles falls within a close range (~ 150 mV @ 500 mA cm^{-2}) as shown in Figure S33f.

In all these cases, we note that the WD overpotential is equivalent to the change in the electric potential across the junction from its equilibrium value as the current is driven.[9] This approximation is valid because the activity, and hence chemical potential, of the proton and hydroxide ionic charge carriers is effectively constant within the bulk CEL and AEL phases, respectively. In a recent study, Rodellar et al. reported that the electrochemical bias can contribute towards the reversible charging of interfacial capacitance in BPM.[26] It is this capacitive charging that changes the total electric potential drop across the AEL/CEL phases, relative to the equilibrium value. The exact three-dimensional electric-potential profile, and hence electric field distribution, however, is an open question and is influenced by both the presence of mobile ions and polarizability in the water phase and by mobile electrons and electronic polarizability in the porous, water-permeated, solid WD-catalyst.

Correlating interfacial catalyst thickness and surface area. After the electrolyzer test, we performed cross-sectional scanning-electron-microscopy (SEM) imaging of catalyst-coated BPMs to measure the thickness of the catalyst layer at each optimal catalyst loading. SEM cross-section images of HfO_2-core-shell catalyst-coated BPM interfaces (Figure 5, and pristine nanoparticle-coated BPM cross sections are in Figure S34). The junction thickness, *at optimal WD catalyst loading*, varied substantially and appears to be a function of the dielectric constant (ε) and/or electronic conductivity (σ). A similar trend is observed with TiO_2-coated reference samples such as TiO_2-coated Ti and TiO_2-coated TiO_2 (Figure S35). A core finding is that conductive cores lead to much larger optimal WD catalyst loading than insulating cores, suggesting a substantial effect of local electric field.

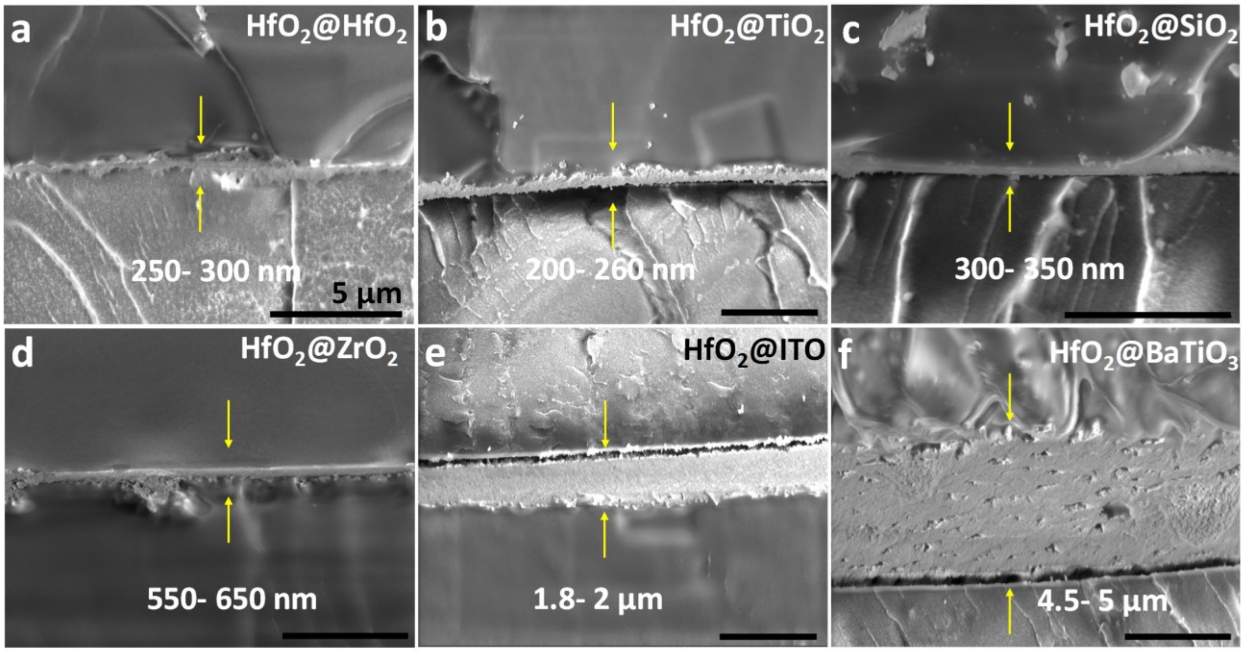

Figure 5: BPM cross-section images of WD catalyst layer after electrolyzer testing. (a) HfO_2@TiO_2 (b) HfO_2@SiO_2, (c) HfO_2@ITO and (d) HfO_2@$BaTiO_3$ catalyst-coated membranes. These HfO_2-coated various core-shell catalysts are at their optimal loading conditions yielding the best electrolyzer performance (500 mA cm^{-2} at cell potential ≈ 3.2 V). Scale bars in the figures are 5 µm.

We also measured the Brunauer-Emmett-Teller (BET) microscopic surface area using N_2 adsorption isotherms of core-shell systems and compare the junction thickness/catalyst loading to normalize data to catalyst surface area (Figure S36 and Table S6). We calculate the amount of catalyst present at the interface and the surface area (available surface sites for WD) at their optimal performance conditions (Section S7b). The ratio between the measured BET surface area to the actual catalyst present (roughness factor) at the BPM interface at optimal loading across the systems for these catalysts falls in a close range (for HfO_2 systems, the ratio is between 26 to 39; for TiO_2 systems, the ratio is 28 to 32).

The BPM WD performance varied with the junction thickness (Figure S37), however, this correlation is convoluted by the available surface area of the WD catalyst. We tested the thickness-dependent activity of catalyst-coated BPM (with a low electronic conducting core, i.e., HfO_2@TiO_2). Once loading increases above the optimal conditions (or optimal surface area), the performance of BPM electrolyzer performance decreases even though there are increasing catalytic sites (supporting Information Figure S37). As per the recent calculation by Mareev et al., increasing the thickness of the interface layer decreases the WD rate at a given overpotential owing to a lower electric field across the interface.[27,28] The poor performance of the BPM electrolyzer in here may be caused by both a weak electric-field across the catalyst layer and increasing ohmic resistance for the ions generated during WD while transporting through thick WD catalyst layers. The ohmic part of the η_{wd} will depend on rates of proton transport via surface-mediated mechanisms on the various metal-oxides surfaces. These appear relatively fast for P25 TiO_2,[9] but haven't been quantified for the other systems and core-shell materials here.

Here we also hypothesize that high electrical conductivity or relative dielectric core materials screen the electric field within the core and enable thicker interfacial catalyst layers without affecting the WD kinetics by concentrating the electric field to the catalyst shell and water interface region.[25,26] A trade-off between the electric field and catalytic effect explains the U-shape dependence of electrolyzer performance on catalyst loading (Figures S26f, S27f, and S28e).

Local electric-field effects on WD. The simulations show, within the approximations used, that a 5 nm thick shell on a conductive core of 20 nm provides a three-fold increase in the field strength at the surface (Figure 1e-g). Further modeling and analysis in Figures S39 and S40 include the ions from WD also show a 3-4-fold enhancement in electric field strength with a conducting core. The effect of the electric field on the WD rate constant $k_{d(E)}$ per Onsager's model is discussed in Section S8.[12] From Onsager's equation, a three-fold enhancement in the electric field with core-shell nanoparticles yields a doubling of $k_{d(E)}$. However, Onsager's model also underestimates the experimental WD rate by $\sim 10^4$ when used alone without consideration of possible mechanisms involving WD catalysts. Calculations by Strathmann and coworkers showed WD from electric-field enhancement via the Onsager model three orders of magnitude less than experimental estimates.[29,30] We note that the concept of the 2nd Wien effect in modulating the rate of WD can be cast more generally in the context of transition-state theory where in this case, the presence of a strong local electric field modulates the energies of precursor, intermediate, and product states. The resulting driving-force-dependent activation energy can be further decomposed into activation entropy and activation enthalpy, both of which can be affected by the local electric field.[26,37,38]

Onsager's model estimates the effect of the local electric field on the dipole formed by the incipient dissociation products. When a dipole is placed in the proximity of a conducting surface, it will also attract opposite electronic charges on the surface (image charge) to lower its free energy. This process leads to Coulombic image-charge interactions between the water dipole, and the induced dipole on the catalyst. The metal oxides under study include highly conducting metal oxides (ex., ITO), and high dielectric metal oxides (ex. $BaTiO_3$), etc. These metal oxides can strongly interact with nearby charge and dipoles (e.g. in water) by deforming their electronic charge distribution in the solid near the particle surface. To illustrate the maximum possible magnitude of this effect, we treat the particle core as a perfect metal and use simple image charge energy calculations. Here we estimate the energy of this image charge configuration and its prospects of affecting the WD kinetics. We assume that the electric field at the BPM interface distorts the water dipole into the Bjerrum state (i.e. where water has started to dissociate and OH^- and H^+ are held together as an incipient ion pair). We don't take the background electric field into account in this image-charge energy estimate, as it is already accounted for, while considering water molecules in the Bjerrum state. The electric potential energy of this dipole-dipole system is calculated as:

$$U = pE \tag{7}$$

where dipole moment $p \sim 3\,D = 10^{-29} C\,m$. Considering a high electric field strength (1 V/Å) that causes a dipole moment to increase around ≈ 1 Debye above the reported 1.84 D for free water.[31,32] In the BPM, the interfacial field could cause an enhancement in the dipole moment of the water molecule (2.9 ± 0.6 D) due to polarization and delocalization effects; hence use the higher value (3 D) for the dipole moment of water in our calculations as Bjerrum dipole.[33]

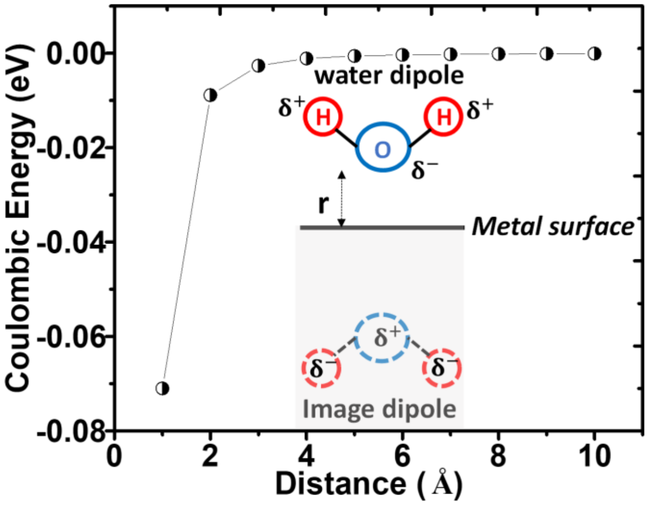

Figure 6: Image charge interactions. The strength of Coulombic attractive interactions between the water dipole and the induced dipole on the surface (due to the presence of the water dipole) as a function of distance from the conducting surface.

The conducting core material will stabilize the water dipole at the catalyst surface through image-charge interactions. We calculated the energy of this image charge configuration by placing the water molecule at different distances (r) above the metal (Section S9). The relative permittivity of the surroundings (interfacial water) is estimated as ε_r = 10 and included in the calculation.[34] The energy of this charge configuration has $\frac{1}{(2r)^3}$ dependence on the distance and falls off rapidly once the distance increases as given in Figure 6.

These simple calculations suggest that image charge will only play a large role in stabilizing the dipole of the water molecule within 1-2 Å of the conducting surface – i.e. within the distance of one atomic bond. For example, the activation energy of the water molecule for WD is found as 15-30 kJ mol^{-1} (0.15-0.30 eV),[17] and the hydrogen bonds free water are ~ 20 kJ mol^{-1} (~ 0.2 eV; at ambient conditions).[35] The energy of the image-charge configuration can be found in such a comparable energy range (~ 0.07 eV) only when the conducting core is employed and the dipole is placed at a very short distance above the surface (r =1 Å). Hence, in the core-shell nanoparticles, the induced dipoles on the semiconducting catalyst shell are likely small and insignificant image-charge interactions to stabilize the Bjerrum state.

This aligns with our experimental finding that catalyst shell coating (≥ 3 nm) masks the core properties from substantially affecting water dissociation kinetics. We have also tested a thinner catalyst shell (TiO_2) on different core nanoparticles (SiO_2, ITO, and ZrO_2) as a WD catalyst. However, the thinner catalyst layer has much different chemical properties based on the XAS data of 1-nm TiO_2 coated onto ZrO_2 and SiO_2 in Figures 3e, 3f, and 3g, probably due to interdiffusion and interface reaction, leading to scattered BPM WD performances (Supporting Information Figure S41). For example, changes in the local chemical structure of the TiO_2 shell due to chemical reaction between the core and shell apparently cause differing WD kinetics in the BPM. Thin coatings on large surface area nanoparticles might also suffer from uneven coverage. These thin layers are also likely to be hydrated and permeable by ionic species in the electrode, making the details of interface electric potential drop difficult to predict and measure (Figure S42).[36]

All these effects require more study to deconvolute and may contribute to the lack of strong acceleration of water dissociation on catalysts with conducting cores and active-shell catalysts. Regardless, the increase in optimal catalyst mass loading is consistent with longer-length scale electrostatic screening effects of the metal cores previously observed in carbon-TiO_2 nanoparticle mixtures. [9,17]

Conclusion

While additional studies are necessary to address the detailed relationship between EFE and catalytic water dissociation in the bipolar junction, this work illustrates that the electric field distribution likely has multiple effects on the water dissociation process. As found previously, [9,17] the presence of metallic (electronically conducting) components to the catalyst modulate the electrostatic field distribution across the entire water dissociation catalyst layer and electronically conductive catalysts have optimal loadings that can be much larger, and thus thicker catalyst films, than those with insulating or semiconductor materials properties. In this way the metal-core/semiconductor-shell particles studied here behave similar to the mixtures of semiconductor and carbon nanoparticles studied earlier.

At the molecular level, the studies here further show that image dipole effects (associated with the metallic core) may directly act on the energy of the dipolar (Bjerrum) transition state. While the shells studied here were not sufficiently thin for this effect to lead to increased WD rates for shells on conductive cores, this effect appears likely of relevance for WD reactions that take place directly on the surface of metal WD catalyst nanoparticles. In this study, thin layers of, for example TiO_2, on metal surfaces failed to show enhanced WD kinetics due the metal core and were instead found to be substantially different chemically from the crystalline TiO_2 counterparts.

In sum, this work adds to the understanding of WD catalysis and design of effect catalysts for ionic processes like proton transfer to/from a surface. In the context of WD: (1) The catalyst should be able to stabilize dipolar transition states associated with proton transfer including via contributions from image-charge attractions, where catalyst electronic conductivity matters on the surface. (2) The catalyst should screen the electric field in the bulk of the catalyst, and provide a sharp electric potential gradient at the catalyst-water interface. (3) Based on our previous studies,[8,39] the catalyst should host large numbers of proton-accepting and proton-donating acid-base reaction sites on its surface. Substantial opportunity to further engineer the density and distribution of proton-binding energies for these sites likely exists. We also emphasize the importance of continued development of theoretical models and accurate simulation approaches to illustrate the molecular details of heterogeneous water dissociation in the presence of a strong electric field and accurately account for the physical properties of WD catalyst including electronic conductivity, dielectric constant, surface proton/hydrogen coverage, etc.

Acknowledgment

This work was initially supported by the U.S. Office of Naval Research, Office of Naval Research grant N00014-20-1-2517 and finished under the U.S. Department of Energy, Office of Science Energy Earthshot Initiative as part of the Bipolar Membrane Science Foundations for the Energy Earthshot under contact #DE-SC0024713. PVS acknowledges the Fulbright-Nehru postdoctoral fellowship supported by the United States-India Educational Foundation (USIEF). The work made use of shared instrumentation in the Center for Advanced Materials Characterization in Oregon (CAMCOR) and the Phil and Penny Knight Campus for Accelerating Scientific Impact. We also acknowledge Dr. Josh Razink for collecting the TEM images. Use of the Advanced Photon Source (Beamline 12-BM), an Office of Science user facility, was supported by the U.S. Department of Energy, Office of Science, Office of Basic Energy Sciences, under Contract DE-AC02-06CH11357.

Author contributions

PVS and S.W.B. designed the experiments and led the project. PVS performed most of the experiments including material synthesis, characterization, and BPM electrolyzer analysis. LHC performed the COMSOL simulation. SS conducted BPM electrolyzer tests of various pristine nanoparticles and developed various reference samples. BVK and LXC conducted and led XAS, and NPW was involved in the XAS discussions. LC, JH, and JM were involved in in-situ XAS measurements. BVK and JH were involved in the diffuse reflectance UV-Vis analysis. MK performed surface area analysis of various nanoparticle systems. The manuscript is written by PVS and SWB by collecting contributions from all the authors.

Supporting Information Available: This material is available free of charge via the Internet at http://pubs.acs.org.

References

(1) Bui, J. C.; Lees, E. W.; Marin, D. H.; Stovall, T. N.; Chen, L.; Kusoglu, A.; Nielander, A. C.; Jaramillo, T. F.; Boettcher, S. W.; Bell, A. T.; Weber, A. Z. Multi-Scale Physics of Bipolar Membranes in Electrochemical Processes. *Nat. Chem. Eng.* **2024**, *1* (1), 45–60. https://doi.org/10.1038/s44286-023-00009-x.

(2) Xie, K.; Miao, R. K.; Ozden, A.; Liu, S.; Chen, Z.; Dinh, C.-T.; Huang, J. E.; Xu, Q.; Gabardo, C. M.; Lee, G.; Edwards, J. P.; O'Brien, C. P.; Boettcher, S. W.; Sinton, D.; Sargent, E. H. Bipolar Membrane Electrolyzers Enable High Single-Pass CO2 Electroreduction to Multicarbon Products. *Nat Commun* **2022**, *13* (1), 3609. https://doi.org/10.1038/s41467-022-31295-3.

(3) Yan, Z.; Wycisk, R. J.; Metlay, A. S.; Xiao, L.; Yoon, Y.; Pintauro, P. N.; Mallouk, T. E. High-Voltage Aqueous Redox Flow Batteries Enabled by Catalyzed Water Dissociation and Acid–Base Neutralization in Bipolar Membranes. *ACS Cent Sci* **2021**, *7* (6), 1028–1035. https://doi.org/10.1021/acscentsci.1c00217.

(4) Vermaas, D. A.; Sassenburg, M.; Smith, W. A. Photo-Assisted Water Splitting with Bipolar Membrane Induced PH Gradients for Practical Solar Fuel Devices. *J Mater Chem A Mater* **2015**, *3* (38), 19556–19562. https://doi.org/10.1039/C5TA06315A.

(5) Seeberger, D.; McLaughlin, D.; Hauenstein, P.; Thiele, S. Bipolar-Interface Fuel Cells – an Underestimated Membrane Electrode Assembly Concept for PGM-Free ORR Catalysts. *Sustain Energy Fuels* **2020**, *4* (5), 2508–2518. https://doi.org/10.1039/D0SE00288G.

(6) Digdaya, I. A.; Sullivan, I.; Lin, M.; Han, L.; Cheng, W.-H.; Atwater, H. A.; Xiang, C. A Direct Coupled Electrochemical System for Capture and Conversion of CO2 from Oceanwater. *Nat Commun* **2020**, *11* (1), 4412. https://doi.org/10.1038/s41467-020-18232-y.

(7) Marin, D. H.; Perryman, J. T.; Hubert, M. A.; Lindquist, G. A.; Chen, L.; Aleman, A. M.; Kamat, G. A.; Niemann, V. A.; Stevens, M. B.; Regmi, Y. N.; Boettcher, S. W.; Nielander, A. C.; Jaramillo, T. F. Hydrogen Production with Seawater-Resilient Bipolar Membrane Electrolyzers. *Joule* **2023**, *7* (4), 765–781. https://doi.org/https://doi.org/10.1016/j.joule.2023.03.005.

(8) Oener, S. Z.; Foster, M. J.; Boettcher, S. W. Accelerating Water Dissociation in Bipolar Membranes and for Electrocatalysis. *Science (1979)* **2020**, *369* (6507), 1099–1103. https://doi.org/10.1126/science.aaz1487.

(9) Chen, L.; Xu, Q.; Oener, S. Z.; Fabrizio, K.; Boettcher, S. W. Design Principles for Water Dissociation Catalysts in High-Performance Bipolar Membranes. *Nat Commun* **2022**, *13* (1), 3846. https://doi.org/10.1038/s41467-022-31429-7.

(10) Newman, J.; Bennion, D.; Tobias, C. W. Mass Transfer in Concentrated Binary Electrolytes. *Berichte der Bunsengesellschaft für physikalische Chemie* **1965**, *69* (7), 608–612. https://doi.org/https://doi.org/10.1002/bbpc.19650690712.

(11) SIMONS, R. Strong Electric Field Effects on Proton Transfer between Membrane-Bound Amines and Water. *Nature* **1979**, *280* (5725), 824–826. https://doi.org/10.1038/280824a0.

(12) Onsager, L. Deviations from Ohm's Law in Weak Electrolytes. *J Chem Phys* **2004**, *2* (9), 599–615. https://doi.org/10.1063/1.1749541.

(13) Simons, R.; Khanarian, G. Water Dissociation in Bipolar Membranes: Experiments and Theory. *J Membr Biol* **1978**, *38* (1), 11–30. https://doi.org/10.1007/BF01875160.

(14) Yan, Z.; Zhu, L.; Li, Y. C.; Wycisk, R. J.; Pintauro, P. N.; Hickner, M. A.; Mallouk, T. E. The Balance of Electric Field and Interfacial Catalysis in Promoting Water Dissociation in Bipolar Membranes. *Energy Environ Sci* **2018**, *11* (8), 2235–2245. https://doi.org/10.1039/C8EE01192C.

(15) Mafé, S.; Ramírez, P.; Alcaraz, A. Electric Field-Assisted Proton Transfer and Water Dissociation at the Junction of a Fixed-Charge Bipolar Membrane. *Chem Phys Lett* **1998**, *294* (4), 406–412. https://doi.org/https://doi.org/10.1016/S0009-2614(98)00877-X.

(16) Blommaert, M. A.; Aili, D.; Tufa, R. A.; Li, Q.; Smith, W. A.; Vermaas, D. A. Insights and Challenges for Applying Bipolar Membranes in Advanced Electrochemical Energy Systems. *ACS Energy Lett* **2021**, *6* (7), 2539–2548. https://doi.org/10.1021/acsenergylett.1c00618.

(17) Lihaokun Chen; Qiucheng Xu; Shannon W Boettcher. Kinetics and Mechanism of Heterogeneous Voltage-Driven Water-Dissociation Catalysis. *Joule* **2023**, *7* (8), 1867–1886. https://doi.org/https://doi.org/10.1016/j.joule.2023.06.011.

(18) Mohanty, A. D.; Tignor, S. E.; Krause, J. A.; Choe, Y.-K.; Bae, C. Systematic Alkaline Stability Study of Polymer Backbones for Anion Exchange Membrane Applications. *Macromolecules* **2016**, *49* (9), 3361–3372. https://doi.org/10.1021/acs.macromol.5b02550.

(19) Evtushenko, Yu. M.; Romashkin, S. V; Trofimov, N. S.; Chekhlova, T. K. Optical Properties of TiO2 Thin Films. *Phys Procedia* **2015**, *73*, 100–107. https://doi.org/https://doi.org/10.1016/j.phpro.2015.09.128.

(20) Angelomé, P. C.; Andrini, L.; Calvo, M. E.; Requejo, F. G.; Bilmes, S. A.; Soler-Illia, G. J. A. A. Mesoporous Anatase TiO2 Films: Use of Ti K XANES for the Quantification of the Nanocrystalline Character and Substrate Effects in the Photocatalysis Behavior. *J. Phys. Chem. C* **2007**, *111* (29), 10886–10893. https://doi.org/10.1021/jp069020z.

(21) Djerdj, I.; Tonejc, A. M. Structural Investigations of Nanocrystalline TiO2 Samples. *J Alloys Compd* **2006**, *413* (1), 159–174. https://doi.org/https://doi.org/10.1016/j.jallcom.2005.02.105.

(22) Gaultois, M. W.; Grosvenor, A. P. XANES and XPS Investigations of (TiO2)x(SiO2)1−x: The Contribution of Final-State Relaxation to Shifts in Absorption and Binding Energies. *J Mater Chem* **2011**, *21* (6), 1829–1836. https://doi.org/10.1039/C0JM03464A.

(23) Li Hsiung, T.; Paul Wang, H.; Wang, H. C. XANES Studies of Photocatalytic Active Species in Nano TiO2–SiO2. *Radiat. Phys. Chem.* **2006**, *75* (11), 2042–2045. https://doi.org/https://doi.org/10.1016/j.radphyschem.2005.11.021.

(24) Mountjoy, G.; Pickup, D. M.; Wallidge, G. W.; Anderson, R.; Cole, J. M.; Newport, R. J.; Smith, M. E. XANES Study of Ti Coordination in Heat-Treated (TiO2)x(SiO2)1-x Xerogels. *Chem. Mater.* **1999**, *11* (5), 1253–1258. https://doi.org/10.1021/cm980644u.

(25) Arpaporn Teamsinsungvon; Chaiwat Ruksakulpiwat; Penphitcha Amonpattaratkit; Yupaporn Ruksakulpiwat. Structural Characterization of Titanium–Silica Oxide Using Synchrotron Radiation X-Ray Absorption Spectroscopy. *Polymers (Basel)* **2022**, *14* (13), 2729.

(26) Rodellar, C. G.; Gisbert-Gonzalez, J. M.; Sarabia, F.; Roldan Cuenya, B.; Oener, S. Z. Ion Solvation Kinetics in Bipolar Membranes and at Electrolyte–Metal Interfaces. *Nat Energy* **2024**, *9* (5), 548–558. https://doi.org/10.1038/s41560-024-01484-z.

(27) Mareev, S. A.; Evdochenko, E.; Wessling, M.; Kozaderova, O. A.; Niftaliev, S. I.; Pismenskaya, N. D.; Nikonenko, V. v. A Comprehensive Mathematical Model of Water Splitting in Bipolar Membranes: Impact of the Spatial Distribution of Fixed Charges and Catalyst at Bipolar Junction. *J Memb Sci* **2020**, *603*, 118010. https://doi.org/https://doi.org/10.1016/j.memsci.2020.118010.

(28) Bui, J. C.; Digdaya, I.; Xiang, C.; Bell, A. T.; Weber, A. Z. Understanding Multi-Ion Transport Mechanisms in Bipolar Membranes. *ACS Appl Mater Interfaces* **2020**, *12* (47), 52509–52526. https://doi.org/10.1021/acsami.0c12686.

(29) Strathmann, H.; Rapp, H.-J.; Bauer, B.; Bell, C. M. Theoretical and Practical Aspects of Preparing Bipolar Membranes. *Desalination* **1993**, *90* (1), 303–323. https://doi.org/https://doi.org/10.1016/0011-9164(93)80183-N.

(30) Strathmann, H.; Bauer, B.; Rapp, H.-J. Better Biopolar Membranes. *Chemtech* **1993**, *23* (6), 25–32.

(31) Harder, E.; Eaves, J. D.; Tokmakoff, A.; Berne, B. J. Polarizable Molecules in the Vibrational Spectroscopy of Water. *PNAS* **2005**, *102* (33), 11611–11616. https://doi.org/10.1073/pnas.0505206102.

(32) Silvestrelli, P. L.; Parrinello, M. Structural, Electronic, and Bonding Properties of Liquid Water from First Principles. *J Chem Phys* **1999**, *111* (8), 3572–3580. https://doi.org/10.1063/1.479638.

(33) Zhu, T.; Van Voorhis, T. Understanding the Dipole Moment of Liquid Water from a Self-Attractive Hartree Decomposition. *J Phys Chem Lett* **2021**, *12* (1), 6–12. https://doi.org/10.1021/acs.jpclett.0c03300.

(34) Paddison, S. J.; Reagor, D. W.; Zawodzinski Jr, T. A. High Frequency Dielectric Studies of Hydrated Nafion®1Presented at the Electrochemical Society Symposium: Processes in Polymers and Polymer|Metal Interfaces, Montreal, 4–9 May 1997.1. *J. Electroanal. Chem.* **1998**, *459* (1), 91–97. https://doi.org/https://doi.org/10.1016/S0022-0728(98)00321-0.

(35) Li, D.; Zhu, Z.; Sun, D.-W. Quantification of Hydrogen Bonding Strength of Water in Saccharide Aqueous Solutions by Confocal Raman Microscopy. *J Mol Liq* **2021**, *342*, 117498. https://doi.org/https://doi.org/10.1016/j.molliq.2021.117498.

(36) Lin, F.; Boettcher, S. W. Adaptive Semiconductor/Electrocatalyst Junctions in Water-Splitting Photoanodes. *Nat Mater* **2014**, *13* (1), 81–86. https://doi.org/10.1038/nmat3811.

(37) Sarabia, F.; Gomez Rodellar, C.; Roldan Cuenya, B.; Oener, S. Z. Exploring Dynamic Solvation Kinetics at Electrocatalyst Surfaces. *Nat Commun* **2024**, *15* (1), 8204. https://doi.org/10.1038/s41467-024-52499-9.

(38) Eigen, M.; De Maeyer, L.; Bernal, J. D. Self-Dissociation and Protonic Charge Transport in Water And. *Proc R Soc Lond A Math Phys Sci* **1997**, *247* (1251), 505–533. https://doi.org/10.1098/rspa.1958.0208.

(39) Sasmal, S.; Chen, L.; Sarma, P. V; Vulpin, O. T.; Simons, C. R.; Wells, K. M.; Spontak, R. J.; Boettcher, S. W. Materials Descriptors for Advanced Water Dissociation Catalysts in Bipolar Membranes. *Nat Mater* **23**, 1421–1427, **2024**.**2024**. https://doi.org/10.1038/s41563-024-01943-8.